COMMUNICATIONS IN SCIENCE AND TECHNOLOGY
Homepage: cst.kipmi.or.id

Synergetic effect of ZnO/NiO nanocomposite on the enhancement of photocatalytic degradation efficiency of dyes molecules

Yurin Karunia Apsha Albaina Iasya[a], Fitri Khoerunnisa[a,*], Sadina Sahitya Dewi[a], Restiani Alia Putri[a], Mita Nurhayati[a,b], Ubed Sonai Fahruddin Arrozi[c], Yessi Permana[d], Murni Handayani[e], Wijayanti Dwi Astuti[f], Oh Wen Da[g], Istifhamy Irnanda[c]

[a]*Department of Chemistry, Indonesia University of Education, Bandung 40154, Indonesia*
[b]*Department of Advanced Science and Technology Convergence, Kyungpook National University, Sangju-si 37224, South Korea*
[c]*Department of Chemistry, Faculty of Mathematics and Natural Sciences, State University of Malang, Malang 65145, Indonesia*
[d]*Inorganic and Physical Chemistry Research Division, Faculty of Mathematics and Natural sciences, Institut Teknologi Bandung, Bandung 40132, Indonesia*
[e]*Research Centre for Advanced Materials, National Research and Innovation Agency (BRIN), Tangerang Selatan 15314, Indonesia*
[f]*Department of Electrical Engineering and Informatics, Vocational College, Universitas Gadjah Mada, Yogyakarta 55281, Indonesia*
[g]*School of Chemical Sciences, Universiti Sains Malaysia, Penang 11800, Malaysia*

Article history:
Received: 23 November 2024 / Received in revised form: 7 January 2025 / Accepted: 26 January 2025

Abstract

The discharge of organic dyes into water systems poses severe risks to human health and aquatic ecosystems. A remarkable technique that is increasingly recognized for dyes degradation is photocatalysis. This work aims to investigate the role of zinc oxide/nickel oxide (ZnO/NiO) nanocomposites in enhancing photocatalytic degradation efficiency of dyes molecules. The nanocomposites were prepared using a simple ultrasonication technique and analyzed through X-ray diffraction (XRD), scanning electron microscopy (SEM), and electrochemical impedance spectroscopy (EIS). The XRD pattern of the ZnO/NiO nanocomposites exhibited characteristic peaks aligned with the ZnO and NiO phases, referring to JCPDS standards. The SEM images of nanocomposites featured the rod and irregular flake-like structures with the average size of 80 nm. The nanocomposites showed the highest dye photodegradation efficiency (RB 93.65% and MO 94.82%) in view of a larger semicircular diameter and lowest band gap energy as verified by Nyquist plot and DFT calculation. These results emphasized the synergistic effect of ZnO/NiO nanocomposites in promoting dye photocatalytic degradation.

Keywords: ZnO/NiO; nanocomposites; photocatalytic; degradation efficiency; dyes molecules

1. Introduction

Organic dyes are extensively utilized across a range of industries, including textiles, leather, cosmetics, plastics, pharmaceuticals, food technology, hair dyeing, paper production, or printing [1]. Methylene blue (MB) [2,3], methyl orange (MO) [4], rhodamine B (RB) [5], and acridine orange (AO) are the textile dyes commonly employed, where they are capable of reducing sunlight penetration and lowering photosynthetic activity, thereby resulting in the reduction of dissolved oxygen levels in aquatic environments [6,7]. The discharge of organic dyes into aquatic systems, due to their cancer-inducing and genotoxic nature, is highly potential to bring severe risks to human health, aquatic organisms, and food chains [8].

Various methods such as adsorption [9], electrolysis [10], ion exchange [11], ozonation [12], chemical oxidation [13], reverse osmosis [14], biodegradation [14], photocatalytic degradation [15], and phytoremediation [16] have been developed for eliminating dye pollutants from wastewater. There is a strong interest in advancing innovation to identify the most key strategies to remove organic dye contamination from industrial discharge.

Photocatalysis is considered as a prominent model of effective methods for breaking down organic dyes [17]. This model is highly commended in terms of its cost-effectiveness, environmentally friendliness, and being free from any secondary pollutants [18]. Semiconductor-based photocatalysis has recently gained prominence in addressing energy crises as it helps to degrade any harmful inorganic and organic pollutants in both water and air [19] by generating highly oxidative (ROS), such as hydroxyl and superoxide radicals that play a critical role in degradation processes.

Metal oxide-based semiconductor materials have been identified as efficient photocatalysts. In particular, ZnO is an outstanding n-type semiconductor in terms of its excellent light

* Corresponding author.
Email: fitri@upi.edu
https://doi.org/10.21924/cst.10.1.2025.1583

absorption capability [20], wide bandgap (~3.2 eV) [20], high exciton binding energy (60 meV) [20], strong photocatalytic activity, high redox potential, non-toxic and environmentally friendly nature, biocompatibility, high electrical and thermal conductivity, optical properties, and affordability [21,22]. It has been proven to effectively degrade various organic dyes pollutants, including MB [23], MO [24], RB [25], and AO [26].

A major drawback of ZnO as a photocatalyst, however, lies in its intricate point-defect structure, which accelerates the recombination of photoinduced electron–hole pairs, thereby diminishing its photocatalytic performance. To address this issue, various ZnO-based composite materials have been developed [17], for instance, by combining ZnO with a different semiconductor material in which a heterojunction structure can be established [27].

Combining ZnO with other metal oxides, such as NiO, is expected to improve catalytic performance. There are some reasons for incorporating NiO into ZnO for photocatalytic applications. Firstly, complementary semiconducting properties through the formation of a p-n heterojunction interface can facilitate the splitting of photogenerated electron-hole pairs by creating an internal electric field that drives electrons toward ZnO and holes toward NiO, thereby resulting in reduced charge recombination. Furthermore, the improved charge carrier dynamic through synergistic effect can reduce the recombination of electron and holes, enhancing the number of active species for photocatalytic reactions. Another reason is that the valence and conduction band edges is tunable to optimize redox reactions in specific photocatalytic reaction, and the last one is that it can enhance stability especially toward photocorrosion during photocatalytic process. [28]. This promotes the generation of ROS, well recognized for their strong oxidative ability to decompose organic dye pollutants in wastewater.

Co-precipitation [29], solvothermal [30], electrochemical deposition [31], hydrothermal [20], sol-gel [32], ultrasonic spraying [20], microwave assisted [33], chemical vapor deposition [34] and green synthesis [2] are the methods used for synthesizing ZnO/NiO nanocomposites that enable to control its particle size, morphology, and composition. Of those methods, ultrasonication is seen as a versatile method to synthesize ZnO/NiO nanocomposites due to enhanced mixing and dispersion level, controlled particle size, improved reaction kinetics, increased surface area, and facilitated structural homogeneity and being ecofriendly [35,36].

In this study, we synthesized ZnO/NiO nanocomposites by applying the facile ultrasonication method. The morphological structure of the ZnO/NiO catalyst was characterized using XRD, FESEM/EDX, EIS, and N_2 adsorption at 77 K. The optical properties and band gap energy of ZnO/NiO nanocomposites were calculated by means of the computational modeling via Density Functional Theory (DFT) calculations with ORCA software. The photocatalytic activity of the ZnO/NiO composites on the decomposition of dye compounds (MO and RB) subjected to UV irradiation was carefully and systematically examined.

2. Materials and Methods

2.1. Materials

Zinc nitrate tetrahydrate ($Zn(NO_3)_2 \cdot 4H_2O$), sodium hydroxide (NaOH), nickel nitrate hexahydrate ($Ni(NO_3)_2 \cdot 6H_2O$), Polyethylene glycol (PEG 6 kDa), ethanol, rhodamine B (RB), and methylene orange (MO) with purity grade of 99.99% were purchased from Merck. Here, no additional purification was necessary prior to the synthesis. The deionized water produced by Thermo Fisher Scientific Pure Water Production Equipment 50129872 was used in the entire study.

2.2. Synthesis of ZnO/NiO Nanocomposites

The ZnO and NiO nanoparticles were synthesized using hydrothermal and co-precipitation methods, respectively, following the previous works [37,38]. Meanwhile, the synthesis of ZnO/NiO was carried out by mixing 100 mL of zinc nitrate solution and 100 mL of nickel nitrate solution at different mole ratio by means of magnetic stirrer (300 rpm, 2 h). To maintain the pH around 7, sodium hydroxide solution (1 M) was added dropwise. The mixture was then ultrasonicated for 2 h (75 kHz; 250 W) at room temperature to ensure thorough mixing and dispersion of the metal precursors. In this step, PEG was added to prevent agglomeration. The mixture, successively, underwent (10000 rpm, 1 hour) and The resulting precipitate was repeatedly rinsed with deionized water to remove any residual reactants and byproducts, prior to be dried in an oven at 90°C overnight to ensure the complete removal of moisture. Following this, the dried powder was calculated at a 650°C for 4 h in a muffle furnace. The synthesized ZnO/NiO are denoted as ZnO/NiO (1:1), ZnO/NiO (1:2), and ZnO/NiO (2:1) corresponding to the molar ratio of zinc nitrate: nickel nitrate at (1:1); (1:2); and (2:1), respectively.

2.3. Characterization of ZnO/NiO Nanocomposites

The X-ray diffractograms of ZnO/NiO nanocomposites were obtained with an aid of Brukker D-8 Advanced Eco X-ray diffractometer in the range of 20° - 80° with a scan rate of 2°/min (Cu Kα radiation, λ= 0.15406 nm, 50 kV, 300 mA). The Fourier Transform Infrared (FTIR) spectra were recorded using FTIR-Shimadzu 8400 in the range of 400-4000 cm^{-1} with a scan rate of 2 cm^{-1}/sec using KBr pellets to analyze the functional group of ZnO/NiO nanocomposites. Meanwhile, the morphology and particle sizes were examined using Field Emission Scanning Electron Microscopes – Energy Dispersive X-ray (FESEM-EDX) type Hitachi S-4800 with accelerating voltage and current (10 kVA). The surface area and pore volume of ZnO/NiO nanocomposites were determined by nitrogen adsorption at 77 K using a Quantachrome Nova 4200e instrument. Prior to do measurement, approximately 100-200 mg of the sample were evacuated at 150°C under vacuum for 4 h. The data were then collected at a relative pressure (P/P_0) of 0.99. The specific surface area was determined through the Brunauer–Emmett–Teller (BET) method, while the pore size distribution was analyzed using the Barrett–Joyner–Halenda (BJH) technique. Furthermore, the charge transfer properties were measured using the Electrochemical Impedance Spectroscopy (EIS) with the Gamry 3000 instrument at the frequency of 100 – 10×10^6 Hz. The EIS results were presented in the form of a Nyquist plot describing a relationship between imaginary impedance (Z") and real impedance (Z'). The optical

analysis and band gap energy was calculated using computational modeling through Density Functional Theory (DFT) with B3LYP hybrid functional and LANL2DZ basis set.

2.4. Photocatalytic Activity of ZnO/NiO Nanocomposites

The photocatalytic activity of nanocomposites was evaluated based on the degradation of MO and RB dyes using UV (200-400 nm) radiations at room temperature. All experiments were carried out by mixing 10 mg of catalysts with 100 mL of 10 ppm dye solution with an aid of a magnetic stirrer for 30 min in the dark condition prior to UV radiation. Later, for 1 hour, the homogeneous mixture was irradiated by UV. The catalyst was then separated from the solution using a centrifuge (10000 rpm, 30 min). The residual solutions were measured with a UV-Vis Vis Hitachi UH5000 Spectrophotometer. The absorbance obtained was calculated in concentration based on the calibration curve (SI Fig.1) at the maximum wavelength of 464.5 and 554 nm for MO and RB, respectively (SI-Fig.1). The removal efficiency was calculated using Eq. (1).

$$\%\ Degradation\ efficiency = ((C_o - C_t)/C_o) \times 100\% \quad (1)$$

3. Results and Discussion

3.1. Structure and Morphology of ZnO/NiO Nanocomposites

The X-ray diffraction (XRD) pattern provided the information about the structure of the synthesized ZnO/NiO nanocomposite. The XRD pattern of ZnO (Fig. 1(a)) revealed the typical diffraction peaks at 31.9° [100], 34.5° [002], 36.4° [1 0 1], 47.5° [102], 56.6° [110], 63.0° [103], 66.3° [200], 67.9° [112], 68,9° [201], 72.6° [004], and 77.0° [202] respectively [39] as the typicality of the wurtzite crystal structure of ZnO [40]. Meanwhile, the diffraction peaks aligned closely with the standard *d*-values from the JCPDS card no. 36-1451 [41]. Here, no diffraction peak was observed at $2\theta < 31°$, indicating the absence of any residual precursors or solvents derived from the synthesis process. In contrast, the typical X-ray diffraction peaks of NiO appeared at 2θ 37.3°, 43.3°, 62.8°, 75.8°, and 79.1 (Fig.1(a)) corresponding to lattice structures [111], [200], [220], [311], and [222], respectively [42] in agreement to the standard (JCPDS card no. 47-1049). These results inferred that hydrothermal and co-precipitation methods were successfully used for synthesizing ZnO and NiO, respectively. Moreover, the X-ray diffractograms of synthesized ZnO/NiO nanocomposites at various mole ratios (Fig. 1(b)) depicted a phase mixture of ZnO with NiO where the diffraction peaks were observed at 2θ 31.9° [100]; 34.5° [002]; 36.4° [004]; 37.2° [202]; 43.2° [102]; 47.7° [110]; 56.7° [220]; 63° [200]; 66.5° [112]; 68.1° [201]; 69.3° [311]; 75.2° [202]; and 77° [222] as the combination peaks originated from ZnO and NiO individually. The slight diffraction peaks were observed due to the interaction of ZnO with NiO in the composites at different composition ratio. This confirmed the successful formation of ZnO/NiO nanocomposite via a facile technique of ultrasonication in solution phase as confirmed by combinatory JCPDS. The characteristic X-ray diffraction peaks for ZnO and NiO exhibited a decrease in intensity upon the formation of ZnO/NiO composites at various composition ratios. Meanwhile, as summarized in SI-Table1, the crystallite size of ZnO, NiO, and ZnO/NiO nanocomposites was calculated using the Debye-Scherrer formula [43]. The crystallite sizes of the individual metal oxides and their composites ranged from 24 to 33 nm. ZnO and NiO here had the average crystallite size of 30 nm and 7 nm, smaller than that of the ZnO/NiO nanocomposites (32.6, 31.3 and 28.3 nm) at mole ratio of ZnO:NiO (1:1), (1:2), and (2:1), respectively. The relationship between crystal size and mole ratio indicated that a higher ZnO ratio in the composite increased the crystal size, while a higher NiO ratio in the composite decreased the crystal size. It also demonstrated that the crystalline structure and morphology of the synthesized ZnO, NiO, and ZnO/NiO nanocomposites corresponded to crystalline planes of the hexagonal and cubic [44].

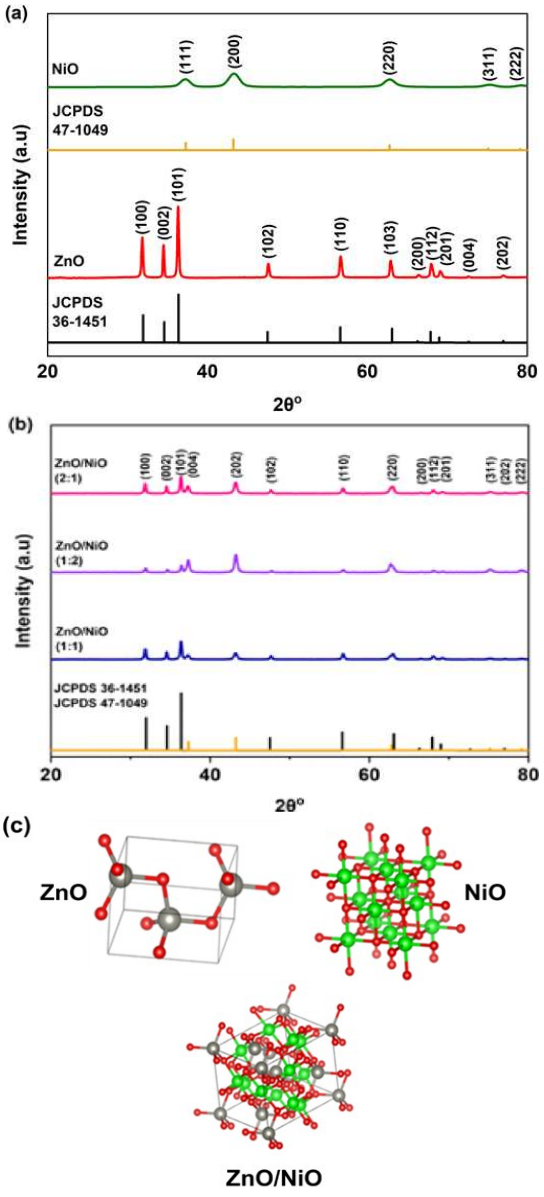

Fig 1. X-ray diffractograms of ZnO and NiO (a), ZnO/NiO nanocomposites (b), and crystal structure (c)

As presented in Fig. 2, the FTIR spectra provided the additional information of ZnO, NiO, and ZnO/NiO

nanocomposites structure. Specifically, a broad peak of FTIR spectra were observed around 3500-3450 cm^{-1} for all metal oxides as a result of the presence of O-H stretching vibrations [45]. The peaks between 2993 cm^{-1} were associated with the C-C sp^3 symmetric and 2400 cm^{-1} asymmetric bending of the C=O bonds from CO_2. Additionally, the band observed between 1740 and 1628 cm^{-1} was attributed to the H-O-H bending vibration of water molecules [46], and the band at 1356 cm^{-1} corresponded to the asymmetrical stretching vibration of nitrate ions. Furthermore, the absorption peak at fingerprint region of 467 cm^{-1} corresponded to the Zn-O bond [47], while the absorption peaks at 701 and 406 cm^{-1} were the characteristics stretching vibrations of Ni-O (SI-Fig.2,3) [48]. Interestingly, the disappearance of peak at 1356 cm^{-1} indicated the conversion of nitrate to oxides [49]. An absorption peak at approximately 550 cm^{-1} demonstrated the characteristic peaks originated from metal-oxygen bonds of Zn-O and Ni-O vibrations for ZnO/ NiO composites. These results confirmed the formation of ZnO, NiO and ZnO/NiO composites.

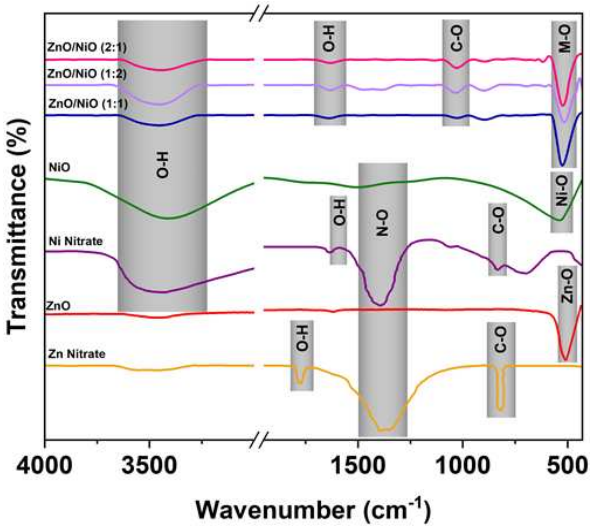

Fig 2. FTIR spectra of ZnO, NiO and ZnO/NiO nanocomposites

Fig. 3 portrays the SEM images regarding the morphology and particle size of the synthesized ZnO/NiO nanocomposites. As shown in Fig.3a, the SEM image of ZnO demonstrated a uniform distribution of particles with rod-like structure with an average particle size of approximately 78.45 nm. This suggested that the use of high temperatures during the hydrothermal process can effectively converts $Zn(NO_3)_2$ into ZnO nanoparticles. Specifically, hydroxyl ions from NaOH reacted with Zn^{2+} ions to form $Zn(OH)_4^{2-}$, as determined by electrostatic forces, prior to undergo a gradual dehydration process. Owing to crystal anisotropy, ZnO growth occurred predominantly along the c-axis, resulting in the formation of ZnO nanorod structures.

The elevated temperatures was found to be capable of promoting more rapid crystal growth in specific directions, particularly along the c-axis of the ZnO nanoparticles' wurtzite structure, supporting the development of rod-like formations [38]. Meanwhile, Fig. 3(b) depicts the morphology and particle size of the synthesized NiO. The SEM image distinctly showed an irregular, flake-like structure created by the clustering of spherical nanoparticles, which adhered to one another, leading to agglomeration [42]. The non-ionic surfactant (PEG), particularly, functioned by binding to the particle surfaces, restricting growth in specific directions, and promoting a spherical morphology with the average particle size distribution of approximately 23 nm.

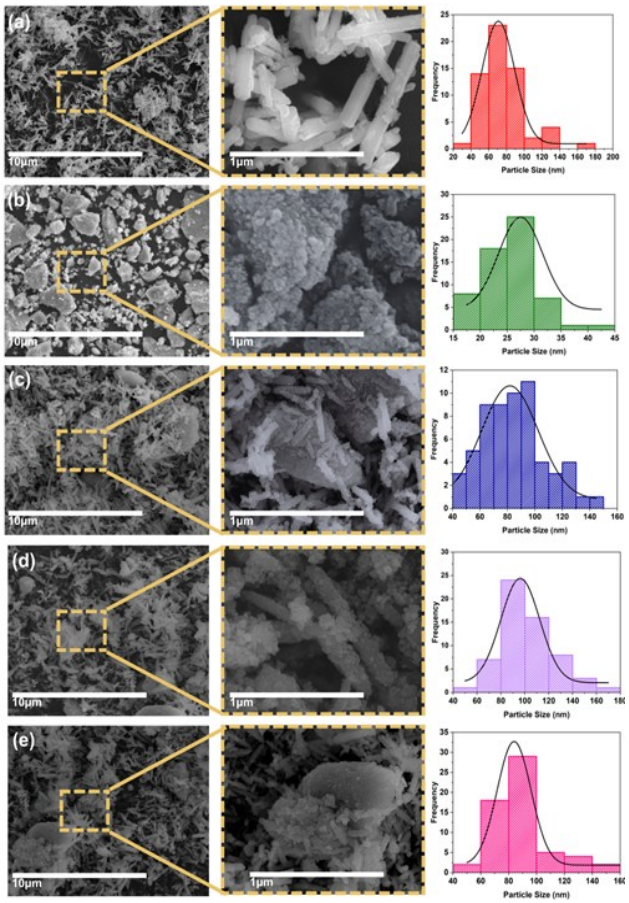

Fig 3. SEM images and particle size distribution of (a) ZnO, (b) NiO, and (c) ZnO/NiO nanocomposites

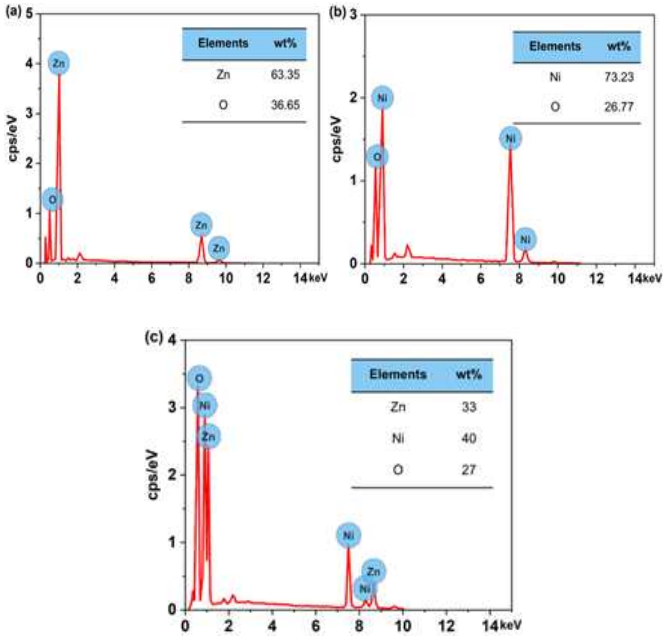

Fig 4. EDX spectra of (a) ZnO, (b) NiO, and (c) ZnO/NiO nanocomposites

Furthermore, the SEM image of the ZnO/NiO nanocomposite revealed a mixed morphology with NiO's spherical structures surrounded by ZnO rods, indicating a homogeneous distribution of NiO and ZnO nanoparticles (Fig. 3(c, d, e)). The ZnO/NiO nanocomposites exhibited a uniform distribution across various mole ratios with an average particle size around 80 nm, slightly larger than that of ZnO nanoparticles. In addition, the EDX spectra, as shown in Fig. 4, displayed the elemental composition (% weight) of ZnO, NiO, and ZnO/NiO nanocomposites, aligning with the weight ratios of each element in the metal oxides. This indicated no impurities present in the synthesized metal oxides, confirming the effective conversion of metal ions to metal oxides.

3.2. Surface Area of ZnO/NiO Nanocomposites

The specific surface area of metal oxides is essential in determining their photocatalytic activity. Commonly, an increased surface area is linked to improved photocatalytic performance, attributed to a greater number of active sites and enhanced charge separation. The specific surface areas of ZnO, NiO, and ZnO/NiO nanocomposites were assessed using nitrogen sorption at 77 K. Fig. 5 illustrates the type IV isotherms featuring a hysteresis loop, indicating that the adsorption and desorption curves were unequal. This behavior is the characteristic of materials with mesoporous structures, suggesting that pore filling and emptying take place at different pressures. It also reflects the physisorption of N_2 molecules into the metal oxide surface, occurred due to van der Waals forces. As the relative pressure rises, the isotherm shows a gradual increase in adsorption as nitrogen fills the pores of the metal oxides. After reaching a specific relative pressure, the adsorption typically levels off, resulting in a plateau that signifies that most of the available adsorption sites (or pores) are occupied, and further increases in pressure do not significantly enhance the amount of nitrogen adsorbed. SI-Table 2 lists the BET (Brunauer, Emmett, and Teller) surface areas, pore volume, and pore radius of ZnO, NiO, and the ZnO/NiO nanocomposite. Specifically, the surface area of ZnO was found smaller than that of NiO, while the surface area of the ZnO/NiO composite fell between those of ZnO and NiO. A similar trend was observed for pore volume; however, the pore radius of the ZnO/NiO composite was found larger than that of the individual metal oxides. This enhanced surface area and porosity were expected to contribute to the performance of the metal oxide composites in photodegradation applications.

Additionally, a higher surface area aided in the effective separation of charge carriers, minimizing recombination rates and enhancing the chances of these charges engaging in chemical reactions. The efficiency of surface reactions, such as oxidation and reduction, was also improved with a larger surface area as it provided more active sites for adsorption and reaction.

3.3. Optical properties and band gap of ZnO/NiO nanocomposites

The efficiency of photocatalytic degradation is highly determined by the band gap energy and optical characteristics of the photocatalysts. A suitable band gap enables the effective light absorption and electron-hole pair generation, while favorable optical properties promote charge separation and reduce recombination rates, ultimately enhancing photocatalytic activity**.** Specifically, charge transfer is a fundamental aspect of photocatalysis, influencing the generation, separation, and utilization of charge carriers. An efficient charge transfer process enhances photocatalytic activity, leading to the improved degradation of pollutants and energy conversion.

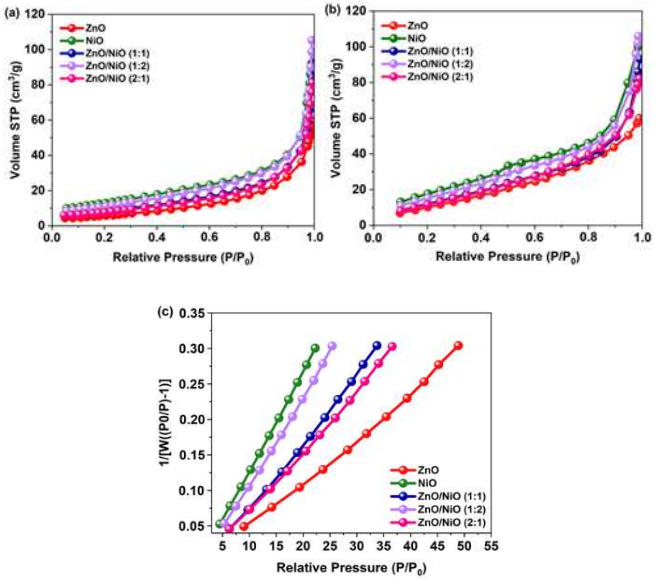

Fig 5. N_2 (a) adsorption, (b) desorption at 77 K, and (c) multiple point of BET

Fig. 6 depicts the Nyquist plots illustrating the charge transfer observed from Electrochemical Impedance Spectroscopy (EIS) Measurements, showing the relationship between the real impedance (Z') and the imaginary impedance (Z") as a function of frequency. These plots displayed the charge transfer resistance in a semicircular pattern for ZnO, NiO, and ZnO/NiO, suggesting that the catalytic mechanism was governed by charge transfer [50]. The ZnO/NiO nanocomposite exhibited a larger semicircle in the Nyquist plot compared to the single metal oxides, reflecting reduced charge transfer resistance, likely due to the improved separation of photogenerated electron–hole pairs [32]. This reduced charge resistance enhanced the electrical conductivity of the catalyst, promoting continuous charge transfer (electrons moving from the valence band to the conduction band) during photocatalysis and ultimately improving the photocatalyst's efficiency.

The band structure and density of states (DOS) for ZnO, NiO, and ZnO/NiO nanocomposites were simulated using Density Functional Theory (DFT). It aimed to determine the catalytic properties by calculating accurate physicochemical values, specifically identifying the HOMO and LUMO energies to determine the band gap (Table. 1). The electronic band gap energies were found at 3.62, 3.60, and 1.59 eV for ZnO, NiO, and ZnO-NiO, respectively. The band gap energy of the ZnO/NiO composite was lower than that of the individual metal oxides. The lowest band gap energy was achieved at a 1:1 composition ratio of ZnO to NiO. However, increasing the

proportion of either ZnO or NiO in the composite increased the band gap energy though it still remained lower than that of the individual metal oxides. The integration of hexagonal ZnO and cubic NiO structures reduced the band gap energy of the nanocomposite. This reduction in band gap energy should enhance the efficiency of photocatalytic degradation [51].

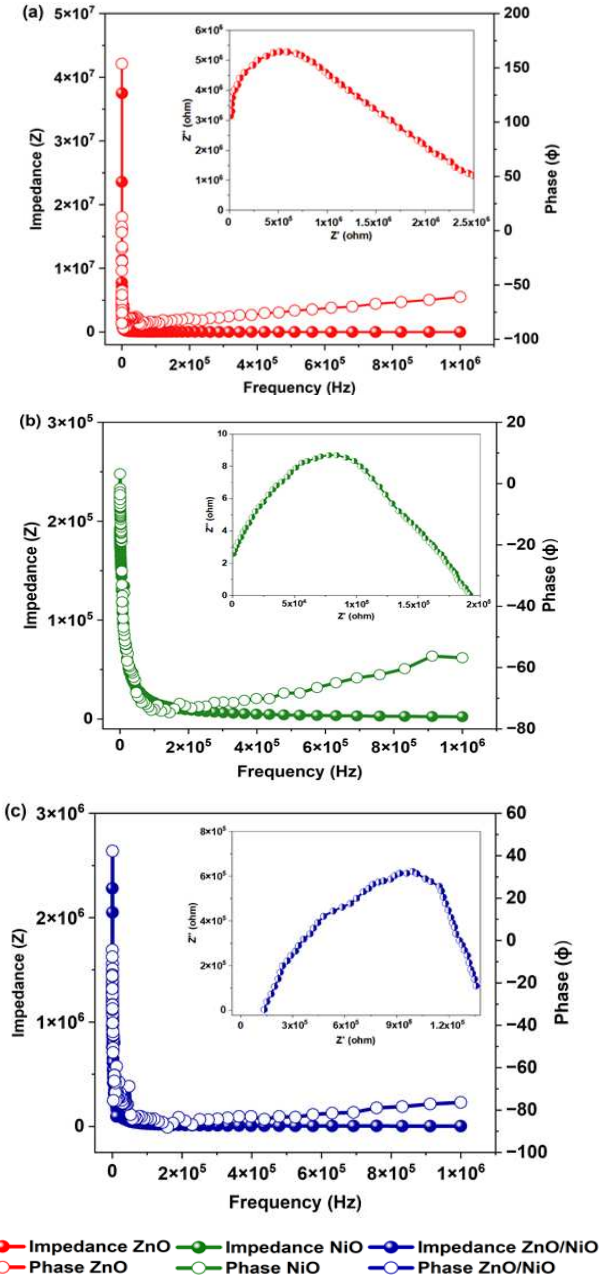

Fig 6. The Nyquist plot of (a) ZnO, (b) NiO and (c) ZnO/NiO nanocomposites

Table 1. Band Gap Energy Values of ZnO, NiO, and ZnO/NiO nanocomposites

ZnO/NiO Ratio	E_{HOMO} (eV)	E_{LUMO} (eV)	Energy Gap (eV)
1:0	-6.59	-2.98	3.62
0:1	-5.40	-1.80	3.40
1:1	-5.44	-3.85	1.59
1:2	-5.50	-3.75	1.76
2:1	-5.78	-3.16	2.62

3.4. Photocatalysis degradation of dyes

The photocatalytic degradation of RB and MO dyes with ZnO/NiO nanocomposites was further investigated under UV light exposure. Fig. 7 illustrates the degradation efficiency of MO and RB dyes using ZnO, NiO, and ZnO/NiO nanocomposites. The results showed that ZnO/NiO nanocomposites achieved higher degradation efficiency than the one in individual metal oxides, indicating a synergistic effect in enhancing degradation activity. The optimum ZnO/NiO composition (1:1) achieved the degradation rates of 93.65% and 94.82% for RB and MO dyes under UV light. Photocatalysts exposed to UV light showed greater degradation efficiency than those not exposed to UV light for each type of catalyst and dye tested. This occurred because UV light promoted dye degradation in photocatalytic processes by supplying the energy needed to activate the photocatalyst. When UV light illuminated the photocatalyst, it then created electron-hole pairs by moving electrons from the valence band to the conduction band.

This process produced highly reactive species, such as hydroxyl radicals (•OH) and superoxide anions (O_2^-•) as. The potent oxidizers capable of breaking down the complex dye molecules into simpler, and less harmful compounds [52]. In contrast, without light, this activation did not occur, thereby leading to the minimal generation of reactive species and significantly lowering dye degradation efficiency.

The ZnO, NiO, and ZnO/NiO nanocomposites demonstrated greater photodegradation efficiency for anionic MO dyes compared to cationic RB dyes, likely due to variations in electrostatic interactions, adsorption properties, and degradation pathways. Specifically, metal oxides developed a positive surface charge in aqueous solutions at pH levels below their point of zero charge (PZC) [53]. This positive charge promoted the adsorption of negatively charged anionic dyes through electrostatic attraction, thereby enhancing their degradation. On the other hand, cationic dyes faced electrostatic repulsion, which decreased their adsorption and hindered their degradation. Moreover, adsorption plays a crucial role in photocatalysis. Anionic dyes tended to adsorb more effectively onto positively charged metal oxide surfaces, allowing greater exposure to reactive species such as hydroxyl radicals (•OH). In contrast, cationic dyes exhibited lower adsorption efficiency, reducing their interaction with the photocatalyst. Additionally, dye degradation depended on reactive oxygen species (e.g., •OH, O_2^-•) with anionic dyes adsorbed on the catalyst surface being directly exposed to these species, enhancing their breakdown. Furthermore, the chemical structures of anionic dyes may make them more vulnerable to attack by reactive oxygen species compared to cationic dyes, further increasing their degradation efficiency. The molecular structure, molecular size, and steric hindrance of dyes molecules should also contribute to the photocatalytic degradation efficiency. The ZnO/NiO (1:1) nanocomposites exhibited the highest degradation efficiency, ascribed to the synergistic effects of reduced band gap energy, altered morphology, and an increased surface area, as evidenced by EIS/DFT computational calculation, X-ray diffraction, SEM N_2 sorption at 77 K, respectively [54]. Table 2 presents a comparison of photocatalytic performance for organic dye

between the present study and previous works. It can be inferred that the ZnO/NiO nanocomposites had the highest photocatalytic degradation efficiency toward dyes molecules within a shortened period compared to others, being superior and promising compared to other catalysts.

Table 2. Comparison of photocatalytic performance of metal oxides on degradation of organic dyes.

Catalysts	Synthesized method	Dyes	Light source	Time (min)	Deg (%)	Ref
ZnO	Sol-gel	MO	UV	180	46	[55]
ZnO	Green Synthesis	MO	UV	180	81	[56]
$CuWO_4$/ ZnO	Precipitation	MO RB	UV	300	91 89	[57]
ZnO/NiO	Solvothermal	RB MO MB	UV	120	72	[58]
Cu/NiO	Hydrothermal	MO MB	Xenon (300 W)	180	72 59	[59]
ZnO/NiO	Ultrasonication	RB MO	UV	60	93 94	This work

3.5. Mechanism of photocatalytic degradation

Fig. 8 represents the mechanism of photocatalytic degradation pathway of RB and MO dyes facilitated by ZnO, NiO, and ZnO/NiO nanocomposites. Upon light irradiation, electrons in the valence band of the metal oxides became excited and transition to the conduction band, leaving positive holes behind. These holes initiated redox reactions on the catalyst surface, primarily by interacting with water molecules (H_2O) or hydroxide ions (OH^-) to generate highly reactive species.

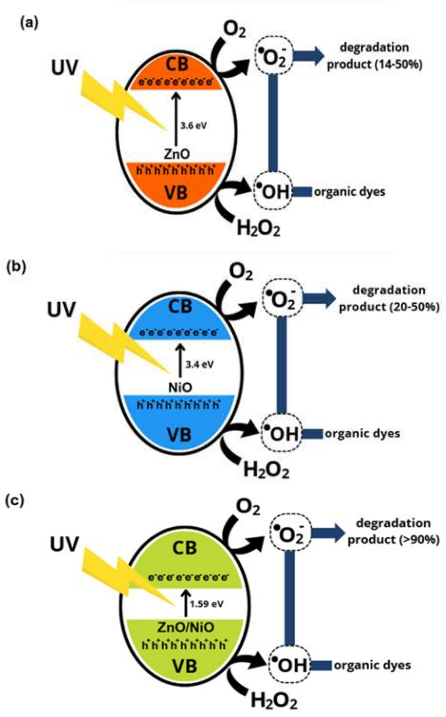

Fig. 8. Plausible mechanism of photocatalytic degradation of dyes using (a) ZnO, (b) NiO, and (c) ZnO/NiO

4. Conclusion

The ZnO/NiO nanocomposites were successfully synthesized using a straightforward ultrasonication method, as evidenced by the Zn-O and Ni-O stretching vibration modes in the fingerprint region, and the combination of X-ray diffraction peaks corresponding to ZnO and NiO nanoparticles, which aligned with the JCPDS standards. The SEM images revealed a mixed morphology of rod-like and irregular flake structures in the ZnO/NiO nanocomposite, derived from ZnO and NiO nanoparticles, respectively with an average size of about 80 nm. The Nyquist plot of ZnO/NiO nanocomposites exhibited a larger semicircular diameter compared to the individual metal oxides, indicating reduced charge resistance, which could be attributed to the separation of photogenerated electron-hole pairs. The band gap energy of ZnO/NiO nanocomposites, calculated via DFT, was found at 1.59 eV, suggesting that these nanocomposites require less energy to excite electrons from the valence band to the conduction band. The ZnO/NiO nanocomposites showed the highest photodegradation efficiency for anionic MO dyes compared to cationic RB dyes, likely due to differences in electrostatic interactions, adsorption behaviors, and degradation mechanisms. These findings highlight the synergistic effect of ZnO/NiO nanocomposites on the enhancement of dye degradation through photocatalysis.

Acknowledgements

We sincerely appreciate the valuable support extended by the Indonesia University of Education through Indonesia Research Collaboration (RKI) Scheme-C (788/UN40.LP/PT.01.03/2024), and International Research Collaboration (62/UN40.D/PT.01.01/2025) grants.

References

1. C. H. Nguyen, R. S. Juang, *Efficient removal of methylene blue dye by a hybrid adsorption–photocatalysis process using reduced graphene oxide/titanate nanotube composites for water reuse*. J. Ind. Eng. Chem. (2019) 296–309.
2. V. Singh, R. Sapehia, V. Dhiman, *Removal of methylene blue dye by green synthesized NiO/ZnO nanocomposites*, Inorg. Chem. Commun. (2024) 162.
3. P. Zhang, D. O'Connor, Y. Wang, L. Jiang, T. Xia, L. Wang, et al. *A green biochar/iron oxide composite for methylene blue removal*, J. Hazard. Mater (2020) 384.
4. B. Sun, Y. Yuan, H. Li, X. Li, C. Zhang, F. Guo, et al., *Waste-cellulose-derived porous carbon adsorbents for methyl orange removal*. Chem. Eng. J. (2019) 55–63.
5. S. Bikerchalen, B. Akhsassi, B. Bakiz, S. Villain, A. Taoufyq, F. Guinneton, et al., *Photocatalytic degradation of Rhodamine B dye over oxygen-rich bismuth oxychloride Bi24O31Cl10 photocatalyst under UV and visible light irradiation: Pathways and mechanism*, J. Phys. Chem. Solids 196 (2025) 112342.
6. S. Marimuthu, A. J. Antonisamy, S. Malayandi, K. Rajendran, P. C. Tsai, A. Pugazhendhi, et al., *Silver nanoparticles in dye effluent treatment: A review on synthesis, treatment methods, mechanisms, photocatalytic degradation, toxic effects and mitigation of toxicity*, J. Photochem. Photobiol. B., 205 (2020).
7. K. P. Sapkota, I. Lee, Hanif MdA, Islam MdA, JR. Hahn. *Solar-Light-*

Driven Efficient ZnO–Single-Walled Carbon Nanotube Photocatalyst for the Degradation of a Persistent Water Pollutant Organic Dye, Catalysts, 9 (2019) 498.

8. M. Adel, M. A. Ahmed, A. A. Mohamed, *Effective removal of cationic dyes from aqueous solutions using reduced graphene oxide functionalized with manganese ferrite nanoparticles*. Compos. Commun., (2020).
9. M. Liu, J. Zheng, L. Wang, Z. Hu, S. Lan, W. Rao, et al., *Ultrafast and selective adsorption of anionic dyes with amine-functionalized glucose-based adsorbents*, J. Mol. Struct. 1263 (2022).
10. Q. Wang, W. Wang, C. Zhu, C. Wu, H. Yu, *A novel strategy to achieve simultaneous efficient formate production and p-nitrophenol removal in a co-electrolysis system of CO_2 and p-nitrophenol*, J. CO_2 Util. 47 (2021).
11. P. He, J. Ding, Z. Qin, L. Tang, K. G. Haw, Y. Zhang, et al., *Binder-free preparation of ZSM-5@silica beads and their use for organic pollutant removal*, Inorg. Chem. Front. 7 (2020) 2080–2088.
12. J. A. Malvestiti, M. R. C. Silva, I. B. de Sousa, R. P. Cavalcante, A. G. C. Quirino, G. C. C. Viana, et al., *Catalytic ozonation using spent battery-based (SB) catalysts for dyes, micropollutant removal and disinfection*, J. Water Process Eng. 65 (2024).
13. H. Yan, C. Lai, D. Wang, S. Liu, X. Li, X. Zhou, et al., *In situ chemical oxidation: Peroxide or persulfate coupled with membrane technology for wastewater treatment*, J. Mater. Chem. A 9 (2021) 11944–11960.
14. H. Chen, X. Zhang, C. Shen, Y. Wang, Z. Li, B. Cao, et al., *Non-thermal plasma degradation of dye wastewater assisted by reverse osmosis process through interfacial mass transfer enhancement*, Chem. Eng. Sci. 282 (2023).
15. J. Lin, D. Gao, J. Zeng, Z. Li, Z. Wen, F. Ke, et al., *MXene/ZnS/chitosan-cellulose composite with Schottky heterostructure for efficient removal of anionic dyes by synergistic effect of adsorption and photocatalytic degradation*, Int. J. Biol. Macromol. 269 (2024).
16. A. A. Adelodun, T. Olajire, N. O. Afolabi, A. S. Akinwumiju, E. Akinbobola, U. O. Hassan, *Phytoremediation potentials of Eichhornia crassipes for nutrients and organic pollutants from textile wastewater*, Int. J. Phytoremediation 23 (2021) 1333–1341.
17. W. M. Naufal, S. Wahyuningsih, W. W. Lestari, *Investigation of hexanal removal through adsorption and photocatalysis on ZIF-7 modified with ZnO, TiO_2, and ZnO/TiO_2 using ATR-FTIR*, Commun. Sci. Technol. 9 (2024) 235–242.
18. P. Wang, X. Zhang, X. Zhang, P. Du, B. Zhou, F. Meng, et al., *Manganese oxide catalytic materials for degradation of organic pollutants in advanced oxidation processes: A review*, J. Water Process Eng. 66 (2024).
19. C. Karthikeyan, P. Arunachalam, K. Ramachandran, A. M. Al-Mayouf, S. Karuppuchamy, *Recent advances in semiconductor metal oxides with enhanced methods for solar photocatalytic applications*, J. Alloys Compd. 828 (2020).
20. Z. Chen, T. Dedova, N. Spalatu, N. Maticiuc, M. Rusu, A. Katerski, et al., *ZnO/NiO heterostructures with enhanced photocatalytic activity obtained by ultrasonic spraying of a NiO shell onto ZnO nanorods*, Colloids Surf. A Physicochem. Eng. Asp. 648 (2022).
21. M. Das, A. Ghatak, P. Guha Ray, U. Stachewicz, *Advancements in ZnO-based photocatalysts for effective rhodamine dye removal from water*, Sustain. Mater. Technol. 42 (2024) e01138.
22. Mankomal, H. Kaur, T. Roy, *Sustainable removal of organic pollutants using biochar based ZnO composites: Experimental and theoretical studies of remediation process*, Surf. Interfaces 49 (2024).
23. Z. Habibollahi, M. Peyravi, S. Khalili, M. Jahanshahi, *ZnO-based ternary nanocomposite for decolorization of methylene blue by photocatalytic dynamic membrane*, Mater. Today Chem. 23 (2022).
24. M. A. Vargas, E. M. Rivera-Muñoz, J. E. Diosa, E. E. Mosquera, J. E. Rodríguez-Páez, *Nanoparticles of ZnO and Mg-doped ZnO: Synthesis, characterization and efficient removal of methyl orange (MO) from aqueous solution*, Ceram. Int. 47 (2021) 15668–15681.
25. J. Godwin, J. R. Njimou, N. Abdus-Salam, P. K. Panda, B. C. Tripathy, M. K. Ghosh, et al., *Nanoscale ZnO-adsorbent carefully designed for the kinetic and thermodynamic studies of Rhodamine B*, Inorg. Chem. Commun. 138 (2022).
26. K. Madeshwaran, R. Venkatachalam, *Green synthesis of bimetallic ZnO–CuO nanoparticles using Annona muricata L. extract: Investigation of antimicrobial, antioxidant, and anticancer properties*, J. Ind. Eng. Chem. (2024).
27. R. Ebrahimi, K. Hossienzadeh, A. Maleki, R. Ghanbari, R. Rezaee, M. Safari, et al., *Effects of doping zinc oxide nanoparticles with transition metals (Ag, Cu, Mn) on photocatalytic degradation of Direct Blue 15 dye under UV and visible light irradiation*, J. Environ. Health Sci. Eng. 17 (2019) 479–492.
28. S. Y. Wu, K. Z. Yuan, X. F. Xu, Z. J. Li, Z. Zhang, P. Wang, et al., *ZnO/NiO coaxial heterojunction nanofibers with oxygen vacancies for efficient photocatalytic Congo red degradation and hydrogen peroxide production*, Ceram. Int. 50 (2024) 39636–39644.
29. P. Muhambihai, V. Rama, P. Subramaniam, *Photocatalytic degradation of aniline blue, brilliant green and direct red 80 using NiO/CuO, CuO/ZnO and ZnO/NiO nanocomposites*, Environ. Nanotechnol. Monit. Manag. 14 (2020).
30. Y. Zhang, J. Zhou, W. Cai, J. Zhou, Z. Li, *Enhanced photocatalytic performance and degradation pathway of Rhodamine B over hierarchical double-shelled zinc nickel oxide hollow sphere heterojunction*, Appl. Surf. Sci. 430 (2018) 549–560.
31. F. Tian, W. Han, J. Hu, H. Wang, H. Li, F. Geng, et al., *Oxygen vacancy-enriched bilayer flower-like structure of ZnO&NiO@C-ZnO nanorod arrays on carbon cloth with improved electrochemical performance*, J. Energy Storage 72 (2023).
32. E. E. El-Katori, E. A. Kasim, D. A. Ali, *Sol–gel synthesis of mesoporous NiO/ZnO heterostructure nanocomposite for photocatalytic and anticorrosive applications in aqueous media*, Colloids Surf. A Physicochem. Eng. Asp. 636 (2022).
33. D. D, A. J. P. P. Winston, S. E, J. M, S. A, *Effective degradation of tetracycline under visible light by microwave-assisted reflux synthesis of ZnO/MoS2/rGO ternary nanocomposites*, Mater. Sci. Semicond. Process. 180 (2024).
34. Y. Jiang, H. Zhang, X. Zuo, C. Sun, Y. Zhang, H. Huang, et al., *Construction of ZnO/Ni@C hollow microspheres as efficient electromagnetic wave absorbers with thin thickness and broad bandwidth*, J. Mater. Sci. Technol. 188 (2024) 62–72.
35. B. Ben Salem, G. Essalah, S. Ben Ameur, B. Duponchel, H. Guermazi, S. Guermazi, et al., *Synthesis and comparative study of the structural and optical properties of binary ZnO-based composites for environmental applications*, RSC Adv. 13 (2023) 6287–6303.
36. S. Yousaf, S. Zulfiqar, M. I. Din, P. O. Agboola, M. F. Aly Aboud, M. F. Warsi, et al., *Solar light irradiated photocatalytic activity of ZnO-NiO/rGO nanocatalyst*, J. Mater. Res. Technol. 12 (2021) 999–1009.
37. F. Aziz, H. M. Abo-Dief, A. Z. Warsi, M. F. Warsi, M. Shahid, T. Ahmad, et al., *Facile synthesis of NiO/ZnO nano-composite by co-precipitation, characterization and photocatalytic study of colored and colorless organic pollutants by solar irradiation*, Physica B Condens. Matter 640 (2022).
38. X. Zhang, L. Zhou, X. Tu, F. Hu, *Hydrothermal synthesis of ZnO crystals: Diverse morphologies and characterization of the photocatalytic properties*, Polyhedron 246 (2023).
39. S. R. Jadhav, S. V. Mohite, K. C. An, D. H. Jang, K. Erande, Y. Kim, et al., *Crafting defective ZnO nanoparticles: A green synthesis for enhanced photocatalytic degradation of organic pollutants*, Ceram. Int. (2024).

40. M. Priyanka, G. S. Reddy, T. R. Kumar Reddy, C. S. Naveen, C. N. S. Kumar, M. Lodhe, et al., *Synthesis and characterization of Y and Mn-doped ZnO nanoparticles: Structural, optical, morphological, and gas sensing investigations*, Physica B Condens. Matter 687 (2024).
41. R. Bairy, P. S. Patil, S. R. Maidur, H. Vijeth, M. S. Murari, U. K. Bhat, *The role of cobalt doping in tuning the band gap, surface morphology and third-order optical nonlinearities of ZnO nanostructures for NLO device applications*, RSC Adv. 9(39) (2019) 22302–22312.
42. O. Baytar, A. Ekinci, Ö. Şahin, S. Kutluay, *Green synthesis of NiO from watermelon seed shell extract for the evaluation of H2 production from NaBH4 hydrolysis and photocatalytic reduction of methylene blue*, Mater. Sci. Eng. B 296 (2023).
43. M. Basak, M. L. Rahman, M. F. Ahmed, B. Biswas, N. Sharmin, *The use of X-ray diffraction peak profile analysis to determine the structural parameters of cobalt ferrite nanoparticles using Debye-Scherrer, Williamson-Hall, Halder-Wagner and Size-strain plot: Different precipitating agent approach*, J. Alloys Compd. 895 (2022).
44. H. T. Handal, W. A. A. Mohamed, A. A. Labib, S. A. Moustafa, A. A. Sery, *The influence of surface modification on the optical and capacitive properties of NiO nanoparticles synthesized via surfactant-assisted coprecipitation*, J. Energy Storage 44 (2021).
45. S. Mallick, M. Nag, D. Bhattacharya, A. Tandi, B. Chakraborty, A. Rao, et al., *Green-synthesized ZnO nanorods as potential deefeblement agent of Pseudomonas aeruginosa and Staphylococcus aureus biofilm*, Biocatal. Agric. Biotechnol. 57 (2024).
46. K. Gupta, B. Sharma, V. Garg, P. P. Neelratan, V. Kumar, D. Kumar, et al., *Enhanced photocatalytic degradation of methylene blue and methyl orange using biogenic ZnO NPs synthesized via Vachellia nilotica (Babool) leaves extract*, Hybrid Adv. 5 (2024) 100160.
47. S. P. Suvaitha, P. Sridhar, T. Divya, P. Palani, K. Venkatachalam, *Bio-waste eggshell membrane assisted synthesis of NiO/ZnO nanocomposite and its characterization: Evaluation of antibacterial and antifungal activity*, Inorg. Chim. Acta 536 (2022).
48. P. Kathiravan, K. Thillaivelavan, G. Viruthagiri, N. Shanmugam, *Investigations of thermal, structural, optical, morphological and magnetic properties of chemical precipitation synthesized NiO nanoparticles for optoelectronic applications*, J. Indian Chem. Soc. 2024 (2024) 101171.
49. A. Mahajan, P. Deshpande, S. Butee, *Synthesis and characterization of NiO/ZnO composite prepared by solid-state reaction method*, Mater. Today Proc. (2021) 1912–1917.
50. M. Kandasamy, A. Husain, S. Suresh, J. Giri, D. J. Jasim, P. Rameshkumar, et al., *Enhanced dye-sensitized solar cell performance and electrochemical capacitive behavior of bi-functional ZnO/NiO/Co3O4 ternary nanocomposite prepared by chemical co-precipitation method*, J. Sci. Adv. Mater. Devices 9(2) (2024).
51. M. F. Sanakousar, C. C. V, V. M. Jiménez-Pérez, B. K. Jayanna, Mounesh, A. H. Shridhar, et al., *Efficient photocatalytic degradation of crystal violet dye and electrochemical performance of modified MWCNTs/Cd-ZnO nanoparticles with quantum chemical calculations*, J. Hazard. Mater. Adv. 2 (2021).
52. J. Zhang, G. Zhang, H. Lan, M. Sun, H. Liu, J. Qu, *Synergetic oxidation of the hydroxyl radical and superoxide anion lowers the benzoquinone intermediate conversion barrier and potentiates effective aromatic pollutant mineralization*, Environ. Sci. Technol. 57(32) (2023) 12117–12126.
53. C. Zhao, B. Wang, B. K. G. Theng, P. Wu, F. Liu, S. Wang, et al., *Formation and mechanisms of nano-metal oxide-biochar composites for pollutants removal: A review*, Sci. Total Environ. 767 (2021).
54. N. R. Ramesh Reddy, P. Mohan Reddy, J. Hak Jung, S. Woo Joo, *Construction of various morphological ZnO-NiO S-scheme nanocomposites for photocatalytic dye degradation*, Inorg. Chem. Commun. 146 (2022).
55. V. V. Pham, T. D. Nguyen, P. P. H. La, M. T. Cao, *A comparison study of the photocatalytic activity of ZnO nanoparticles for organic contaminants degradation under low-power UV-A lamp*, Adv. Nat. Sci. Nanosci. Nanotechnol. 11(1) (2020) 15005.
56. A. Villegas-Fuentes, H. E. Garrafa-Gálvez, R. V. Quevedo-Robles, M. Luque-Morales, A. R. Vilchis-Nestor, P. A. Luque, *Synthesis of semiconductor ZnO nanoparticles using Citrus microcarpa extract and the influence of concentration on their optical properties*, J. Mol. Struct. 1281 (2023).
57. Y. Koedsiri, P. Amornpitoksuk, C. Randorn, T. Rattana, S. Tandorn, S. Suwanboon, *S-Schematic CuWO4/ZnO nanocomposite boosted photocatalytic degradation of organic dye pollutants*, Mater. Sci. Semicond. Process. 177 (2024).
58. N. R. Ramesh Reddy, P. Mohan Reddy, J. Hak Jung, S. Woo Joo, *Construction of various morphological ZnO-NiO S-scheme nanocomposites for photocatalytic dye degradation*, Inorg. Chem. Commun. 146 (2022).
59. R. Amrollahi, *Comparison of photocatalytic activity of Cu/TiO2, Cu/NiO and Cu/ZnO nanocomposites for the degradation of organic dyes*, Appl. Catal. O: Open 195 (2024) 2070.